BMC Oral Health

RESEARCH

Open Access

Surface activation of Ti6Al4V via vacuum versus conventional ultraviolet photofunctionalization: physicochemical and biological insights

Mohamed Ahmed Alkhodary[1*], Ali Alenezi[1], Bandar Awadh Alresheedi[1], Naji Alharethi[1], Rawan Alrethia[1], Abeer Mohamed Ettesh[2] and Ramy Elmoazen[3,4]

Abstract

Background Ultraviolet (UV) photofunctionalization has been proposed as a means of removing hydrocarbon accumulation, which causes aging of titanium surfaces. Recent vacuum–UV (VUV) technologies exhibit faster, and more efficient surface activation compared with conventional UV protocols. The aim of the current work was to compare surface rejuvenation of grade V titanium alloy (Ti–6Al–4 V) using conventional UV and VUV photofunctionalization with physicochemical analyses and biological assays.

Methods Ti6Al4V discs were divided into four groups: Group I (control), Group II (12 min TheraBeam Super Osseo), Group III (15 min TheraBeam Affiny), and Group IV (20 s DIO UV Activator). Surface characteristics were evaluated with SEM, EDS, XRD, TOF-SIMS, and contact angle goniometry. Human bone marrow mesenchymal stem cells (BM-MSC/TERT292) were cultured on discs. Cell viability (MTT), morphology (confocal microscopy, SEM), ALP activity, and osteogenic gene expression (Runx2, BSP, OPN, OCN) were assessed.

Results AFM revealed no changes in surface roughness across groups. EDS, XRD, and TOF-SIMS confirmed progressive hydrocarbon removal with UV treatment, with Groups III and IV showing the lowest carbon levels ($p < 0.001$ vs. control). The contact angle decreased significantly from 76.9° ± 2.58 in controls to 26.9° ± 1.04 after VUV activation ($p < 0.001$). Biologically, UV treatment enhanced proliferation, cytoskeletal organization, ALP activity, and osteogenic gene expression, with Groups III and IV showing significantly greater responses compared with Group II ($p < 0.001$) though not significantly different from each other.

Conclusion Both conventional UV and VUV photofunctionalization rejuvenated titanium surfaces and improved osteogenic responses. VUV devices, particularly the DIO UV Activator, achieved equivalent activation in seconds compared with several minutes with conventional UV, suggesting a clinically advantageous, rapid chairside application.

Keywords Ultraviolet, Photofunctionalization, Titanium, In vitro study

*Correspondence:
Mohamed Ahmed Alkhodary
ma.alkhodary@qu.edu.sa
[1]Present address: Department of Prosthetic Dental Sciences, College of Dentistry, Qassim University, Buraydah, Saudi Arabia
[2]College of Pharmacy and Dentistry, Buraydah Private Colleges, Buraydah, Qassim province, Saudi Arabia
[3]School of Computing, University of Eastern Finland, Yliopistokatu 2, Joensuu 80100, Finland
[4]Egyptian Dental Syndicate, Alexandria, Egypt

© The Author(s) 2026. **Open Access** This article is licensed under a Creative Commons Attribution-NonCommercial-NoDerivatives 4.0 International License, which permits any non-commercial use, sharing, distribution and reproduction in any medium or format, as long as you give appropriate credit to the original author(s) and the source, provide a link to the Creative Commons licence, and indicate if you modified the licensed material. You do not have permission under this licence to share adapted material derived from this article or parts of it. The images or other third party material in this article are included in the article's Creative Commons licence, unless indicated otherwise in a credit line to the material. If material is not included in the article's Creative Commons licence and your intended use is not permitted by statutory regulation or exceeds the permitted use, you will need to obtain permission directly from the copyright holder. To view a copy of this licence, visit http://creativecommons.org/licenses/by-nc-nd/4.0/.

Introduction

Successful dental implant treatment relies on rapid and stable osseointegration, which can be improved by optimizing implant materials and surface modifications to enhance biological interactions at the bone–implant interface. Grade V titanium alloy (Ti6Al4V) is widely used in dental implants due to its favorable mechanical properties and biocompatibility [1–3]. The surface of grade V titanium is known to have good corrosion resistance, and its topography, chemistry, and energy directly influence protein adsorption, osteoblastic adhesion, and subsequent osseointegration [4]. However, titanium surfaces are susceptible to hydrocarbon contamination during storage and handling, leading to a phenomenon known as biological aging, which presents a challenge to bone healing [5, 6]. Such contamination aging results from storage and handling, and decreases surface energy and wettability, leading to impaired protein adsorption and reduced integrin-mediated cell adhesion, which in turn may affect early osseointegration, and delay clinical stability [7, 8].

Ultraviolet (UV) photofunctionalization has been proposed to counteract the effects of titanium aging by improving its physicochemical properties and enhancing its biological responses [9–11]. UV light, particularly in the UVC range, rejuvenates the surface by decomposing its organic contaminants, improves its hydrophilicity, and restores its capacity for protein adsorption, cell adhesion, and osteogenic differentiation [12–14]. In addition, it was found to reduce the early risk of bacterial adhesion [1, 2, 15]. UV photofunctionalization provides photocatalytic oxidation which breaks down the hydrocarbon chains and releases volatile by-products [16]. The process modifies the surface charge, leading to reducing the water contact angle, and creating superhydrophilicity state [17–19]. Surface chemistry analysis techniques demonstrated that UV-treated titanium had significantly reduced carbon-related signals [9, 20].

Several in vitro studies have shown that growth and differentiation of osteoblast-like cells on UV-activated titanium surfaces are markedly enhanced, with reports of 2–4-fold increases in alkaline phosphatase (ALP) activity, and significant upregulation (up to 200–300%) in osteogenic gene expression, including Runx2, osteocalcin, and bone sialoprotein, compared with untreated controls [14, 15, 21, 22]. In addition, cell attachment assays demonstrated nearly complete cell spreading within 24 h and up to 3 times higher initial cell adhesion, reflecting improved surface bioactivity [14, 15]. On the other hand, in vivo studies have demonstrated substantial improvements in bone-to-implant contact (BIC), increasing from approximately 45–55% in untreated implants to 70–85% following UV treatment, along with significantly higher removal torque values (up to 1.5–2 times greater), indicating stronger mechanical fixation and accelerated osseointegration [18, 19, 23–25]. These findings collectively confirm that UV photofunctionalization not only enhances early biological responses but also translates into clinically relevant improvements in implant stability.

Currently, UV photofunctionalization protocols typically require 12–15 min of chairside exposure using dedicated devices, which, although considerably shorter than earlier protocols requiring several hours to days, still represents a time-sensitive procedural step that may interrupt clinical workflow and limit routine adoption [26–31]. Moreover, the need for immediate use after treatment to prevent recontamination further adds logistical constraints [28, 29]. In contrast, recent advances in vacuum-ultraviolet (VUV) technology have demonstrated that comparable hydrocarbon removal and superhydrophilicity can be achieved within as little as 1 min, due to the higher photon energy and enhanced photochemical efficiency [13, 22, 25, 32–34]. This substantial reduction in treatment time may overcome one of the main disadvantages of conventional UV protocols, making photofunctionalization more feasible for widespread clinical implementation. Accordingly, the present study aims to compare the effects of conventional UV and VUV photofunctionalization on sandblasted and acid-etched Ti–6Al–4 V discs, using a combination of analytical techniques and biological assays [35–42].

Materials and methods

UV photofunctionalization devices

Three ultraviolet (UV) activation devices (Fig. 1) were used for implant surface photofunctionalization in the current work, namely, a TheraBeam Super Osseo, a TheraBeam Affiny, and a DIO UV Activator. A comparison of their wavelengths, technology, classification, applications, advantages, limitations, and typical exposure times is presented in (Table 1). Exposure times were selected based on manufacturer recommendations and prior studies [13, 22, 25, 32–34]. All devices were calibrated and used according to manufacturer recommendations.

Titanium sample preparation

Grade V titanium alloy (Ti6Al4V) Sandblasted and dual-acid-etched macro/microtopographies are considered the gold standard in contemporary clinical implant dentistry due to their well-documented ability to facilitate robust biomechanical interlocking and long-term osseointegration. Grade V titanium alloy (Ti6Al4V) (Ruilai Metal Materials Co., Ltd., Baoji, China) was custom-fabricated into disc-shaped specimens with a diameter of 5 mm and a thickness of 1 mm. The discs were sequentially ground using 1200-grit silicon carbide (SiC) abrasive paper under continuous water irrigation to obtain

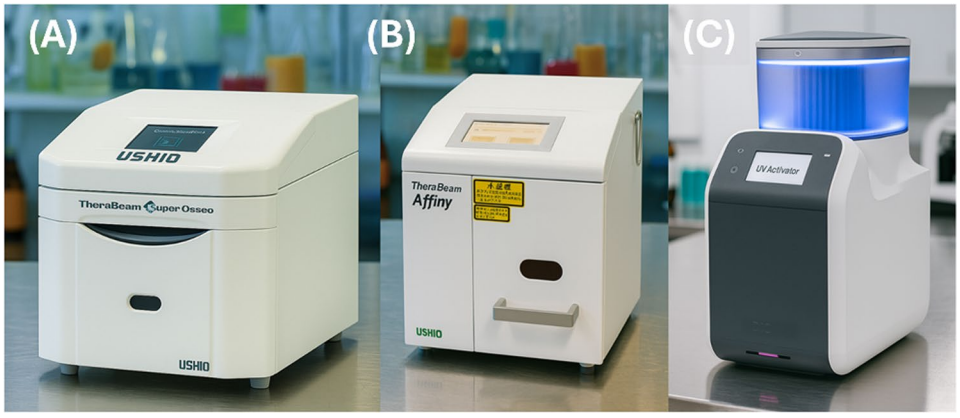


Fig. 1 UV radiation devices: (**A**) TheraBeam Super Osseo. **B** TheraBeam Affiny. **C** DIO UV Activator

Table 1 Comparison of UV activation devices

Device	Manufacturer	UV Wavelength	Light Source	UV Category	Exposure Time
TheraBeam Super Osseo	USHIO, Japan	~250 nm (UVC) + ~360 nm (UVA)	Proprietary mixed-spectrum UV lamps	Proprietary UV (PUV)	12 min
TheraBeam Affiny	USHIO, Japan	172 nm	Xenon excimer lamp (VUV source)	Vacuum UV (VUV)	15 min
DIO UV Activator	DIO Corp., South Korea	172 nm	Xenon excimer lamp (VUV source)	Vacuum UV (VUV)	20 s

a standardized baseline surface. Sandblasting was performed using aluminum oxide (Al_2O_3) particles with an average size of 250–300 µm, delivered at a pressure of 0.4 MPa, at a distance of 10 mm, and for a duration of 15 s per disc, ensuring uniform surface roughening. The specimens were then ultrasonically cleaned in distilled water for 5 min to remove residual blasting particles [16, 21].

Following sandblasting, the discs underwent dual-acid etching using a mixture of concentrated sulfuric acid (H_2SO_4, 95%) and hydrochloric acid (HCl, 36%) in a 1:1 volume ratio. The discs were immersed in the acid solution at a controlled temperature of 60 °C for 30 min, under gentle agitation to ensure uniform etching. This process was used to generate a micro-roughened surface topography and enhance surface energy [16, 17, 21].

After acid treatment, the discs were rinsed thoroughly with distilled water and subjected to ultrasonic cleaning in distilled water for 5 min (twice) to ensure complete removal of residual acids. This was followed by washing in a laboratory-grade detergent solution, an additional ultrasonic cleaning cycle in distilled water for 5 min and drying under sterile conditions in a laminar flow hood. The specimens were sterilized using dry heat at 160 °C for 2 h and subsequently stored in sterile containers under dark conditions at room temperature for 4 weeks to allow for biological aging and hydrocarbon accumulation on the titanium surface [5–8, 28].

Study groups

The discs were divided into four groups:

1. Group I (control): Unexposed to UV radiation.
2. Group II (PUV): Exposed to 12 min of UV radiation in the TheraBeam Super Osseo device (Ushio, Japan).
3. Group III (VUV-15): Exposed to 15 min of UV radiation in the TheraBeam Affiny device (Ushio, Japan).
4. Group IV (VUV-20s): Exposed to 20 s of UV radiation in the DIO UV Activator device (DIO Implant, South Korea).

The following analyses, as seen in Fig. 2, were conducted to investigate the effects of UV photofunctionalization [21, 23, 24, 26, 29] on the titanium discs surfaces:

1. Examination of surface roughness using atomic force microscopy (AFM) quantitative surface roughness parameters, Ra (arithmetical mean roughness) and Rq (root mean square roughness).
2. Chemical composition analysis using energy-dispersive X-ray spectroscopy (EDS), X-ray diffraction (XRD), and Time-of-flight secondary ion mass spectrometry (TOF-SIMS).
3. Wettability analysis using a goniometer.
4. Cell culture analysis of human bone marrow mesenchymal stem cells (BMSCs).

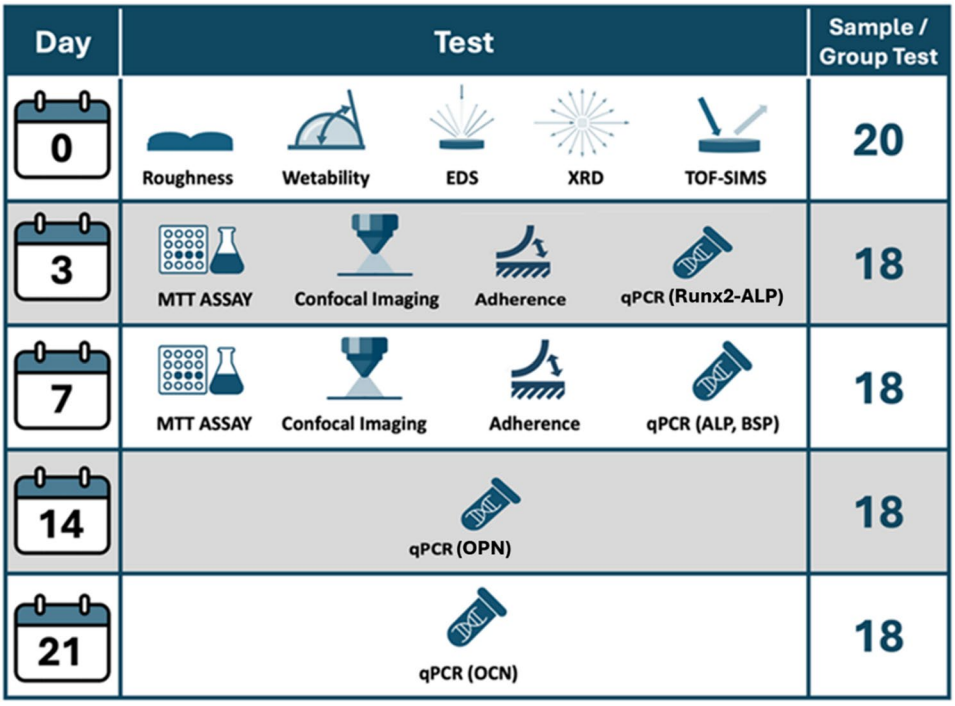


Fig. 2 Experimental design and number of samples used in each test as determined using power analysis

A. MTT assay on days 3 and 7 of cell culture.
B. Laser confocal microscope imaging on days 3 and 7 of cell culture.
C. Scanning electron microscope study of cell adherence patterns on the titanium discs on days 3 and 7.
D. Testing the gene expression of the cells using real-time quantitative polymerase chain reaction (qPCR):
    a) Early: Runx2, ALP on day 3 of cell culture.
    b) Intermediate: ALP and BSP on day 7 of cell culture.
    c) Late: OPN on day 14 and OCN on day 21 of cell culture.

Sample size was determined a priori using GPower software (version 3.1.9.6 for Mac; Heinrich-Heine-Universität Düsseldorf, Germany) for a one-way fixed-effects ANOVA with four independent groups. Based on a large effect size (Cohen's f = 0.40), derived from prior studies reporting 2–4 fold increases in alkaline phosphatase activity and significant upregulation of osteogenic gene expression following UV photofunctionalization of titanium [14, 15, 32], with $\alpha = 0.05$ and statistical power $(1 - \beta) = 0.80$, the analysis yielded a minimum required total sample size of 76 specimens (noncentrality parameter $\lambda = 12.16$; critical F = 2.73; numerator df = 3; denominator df = 72; actual power = 0.82). Accordingly, $n = 18$ specimens per group were used for biological assays, and $n = 20$ per group for surface characterization assays to account for measurement variability and ensure valid comparisons. The sample sizes are consistent with comparable in vitro studies assessing surface modification effects on mesenchymal stem cell behavior and titanium surface chemistry.

Surface characteristics

Surface roughness

Surface roughness was evaluated via observation of the surfaces of 20 samples from each group using Atomic Force Microscopy (AFM) (Nanosurf, Liestal, Switzerland, NaioAFM), using a probe tip smaller than 10 nm radius at 300 kHz, a 40 N/m constant force, a scan area of 10 × 10 μm^2, and an image resolution of 512 × 512 pixels in 3 different spots per sample as in [16–18].

Chemical composition

The elemental composition of 20 titanium surfaces from each group was analyzed using energy-dispersive X-ray spectroscopy (EDS; S4800, Hitachi, Japan) to quantify surface carbon and oxygen levels. Carbon content was used as an indicator of surface hydrocarbon contamination, whereas oxygen levels reflected the degree of titanium and aluminum oxide formation. In addition, X-ray diffraction (XRD; D/MAX-1200, Rigaku, Japan) was performed to evaluate the crystallographic structure of the surfaces. The XRD acquisition parameters were as follows: Cu Kα radiation (λ = 1.5406 Å), operating at 40 kV and 30–40 mA, over a 2θ range of 20°–80°, with a step size of 0.02° and a scan speed of 1°–2°/min. For

semi-quantitative analysis, raw XRD patterns were first subjected to background subtraction using a polynomial fitting method to eliminate noise and baseline drift. The diffraction profiles were then normalized to the total integrated intensity of the entire scan range (20°–80° 2θ) to allow comparison between samples independent of absolute signal intensity. Peak integration was performed using peak analysis software by calculating the area under the curve (AUC) of selected peaks, specifically the broad amorphous carbon-related band (typically observed around 20°–30° 2θ) and characteristic crystalline titanium peaks. Peak areas were determined by fitting the peaks with a Gaussian–Lorentzian function to accurately resolve overlapping contributions. The relative amount of amorphous carbon was expressed as the ratio of the integrated intensity of the carbon-related peak to the total integrated intensity, and these values were further normalized to the control group (untreated samples), which was set to 100% for comparative purposes. This approach enabled semi-quantitative assessment of surface carbon reduction following different treatments. Furthermore, time-of-flight secondary ion mass spectrometry (TOF-SIMS; TOF.SIMS 5, M6) was employed to detect and confirm trace levels of molecular carbon contamination on the titanium surfaces [16–19].

Wettability

Wettability of 20 surfaces from each group was evaluated at room temperature (23 ± 1 °C) using a goniometer (200-F1-230, Ramehart) [17, 18]. A 2 µL double-distilled water droplet was placed on each surface, and the contact angle was measured within 30 s of droplet placement. Contact angles were measured from both left and right sides of the droplet, and the average value was recorded.

Cell culture

An immortalized human bone marrow–derived mesenchymal stem cell line (BM-MSC/TERT292) was obtained from Evercyte (Vienna, Austria). The titanium discs were placed individually into 12-well tissue culture plates, with six discs (n = 6) per experimental group used for each assay. Cells were seeded onto the discs at a density of 1 × 10^4 cells/cm^2 (Fig. 3) in 1 mL of culture medium per well. The culture medium consisted of Dulbecco's Modified Eagle Medium (DMEM; GIBCO, Invitrogen Corp.) supplemented with 10% heat-inactivated fetal bovine serum (FBS), 100 IU/mL penicillin, and 20 µg/mL streptomycin. Cells were maintained in a humidified incubator at 37 °C with 5% CO_2 (Cytoperm® Heraeus®). Each experimental condition was performed in triplicate (three independent experiments) to ensure reproducibility. Cells were initially cultured under basal conditions for 6–12 h to allow for attachment to the titanium discs. Subsequently, osteogenic differentiation was induced by supplementing the culture medium with dexamethasone (100 nM), ascorbic acid-2-phosphate (50 µg/mL), and β-glycerophosphate (10 mM). The osteogenic medium was replaced every 3 days, and the cells were maintained under these conditions for 21 days to promote differentiation [35–42].

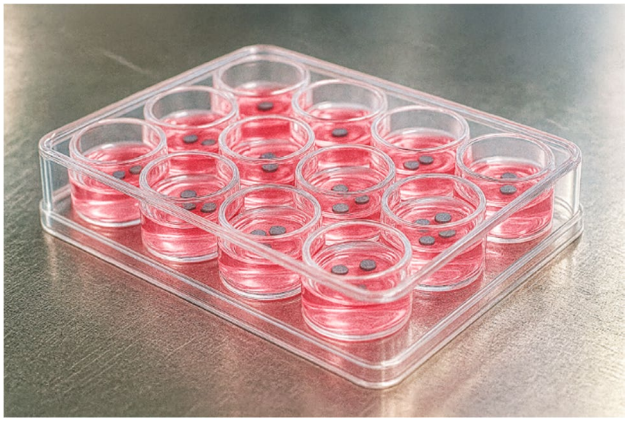


Fig. 3 Cell culture procedures: 12-well plate in a CO_2 incubator

MTT assay

The MTT (3-[4,5-dimethylthiazol-2-yl]-2,5 diphenyl tetrazolium bromide) assay was used for the investigation of cell proliferation after an incubation on days 3 and 7. The MTT reagent formazan was dissolved with solubilization solution (isopropanol and 0.04 N HCl, Sigma), and the cell culture media were replaced with MTT reagent (0.5 mg/mL in serum-free medium) and incubated for three hours at 37 °C. Optical density (OD) was measured at 540 mm using an ELISA reader to obtain the number of cells adhering to each disc.

Confocal laser scanning microscope

Cell morphology and spreading on titanium surfaces were evaluated using a confocal laser scanning microscope (LSM900 Airyscan 2, ZEISS, Germany). For each experimental group, six discs (n = 6) were analyzed per time point, and three independent experiments were performed. At days 3 and 7, cells were gently rinsed twice with phosphate-buffered saline (PBS, 1×, 1 mL per well) and fixed with 4% paraformaldehyde (PFA, 1 mL per well) for 30 min at room temperature. Following fixation, samples were washed three times with PBS (5 min each wash) and permeabilized using 0.1% Triton X-100 in PBS (1 mL per well) for 10 min at room temperature. After permeabilization, non-specific binding sites were blocked with 1% bovine serum albumin (BSA) in PBS (1 mL per well) for 30 min. For cytoskeletal staining, cells were incubated with rhodamine–phalloidin (Beyotime, Shanghai, China; diluted 1:200 in PBS, final concentration ≈ 5 U/mL, 500 µL per well) for 30 min at room temperature

in the dark. Nuclei were counterstained using DAPI (Solarbio, Beijing, China; 1 μg/mL in PBS, 500 μL per well) for 5 min. Where applicable, Alexa Fluor 488-conjugated secondary antibody (Abways, Shanghai, China) was applied at a 1:200 dilution (500 μL per well) and incubated for 1 h at room temperature in the dark, followed by three PBS washes. After staining, samples were mounted using an antifade mounting medium and kept protected from light until imaging. Confocal imaging was performed using a 63× oil immersion objective (NA 1.4). The excitation/emission settings were 405 nm/420–480 nm for DAPI, 488 nm/500–550 nm for Alexa Fluor 488, and 561 nm/570–620 nm for rhodamine–phalloidin. Images were acquired with a pinhole set to 1 Airy unit, a frame size of 1024 × 1024 pixels, and a pixel size of approximately 0.1–0.2 μm. Laser power and detector gain were kept constant across all groups to ensure comparability. Z-stack imaging was performed with a step size of 0.5–1 μm where needed, and maximum intensity projections were generated for analysis. For each disc, at least five random, non-overlapping fields of view were captured, resulting in a minimum of 30 images per group per time point. All image acquisition parameters were kept identical across groups and time points to allow for direct comparison.

Quantitative morphological analysis

After fixation, staining, and confocal image acquisition, the images were segmented for cell identification based on their nuclear fluorescence utilizing the image processing software ImageJ, which automatically measured numerous geometric parameters for each cell as a region of interest (ROI). The geometric parameters were the projected cell area, which is the total number of pixels within the segmented ROI; the aspect ratio, which is the ratio of the major axis to the minor axis of the cell's fitted ellipse; and the circularity, which measures how close the cell shape is to a perfect circle. These parameters reflected cell spreading and shape, which are often correlated with osteogenic differentiation and substrate adhesion.

Confocal microscope images were processed as follows:

1. Pre-processing and noise reduction

   a) Deconvolution to restore blurred light.

   b) Filtering to smooth out high-frequency noise while preserving cell boundaries.
   c) Background subtraction to remove uneven background illumination.

2. Segmentation

   Individual cells were separated from the background and each other for analysis.
   a) Adaptive thresholding as intensity varied across the field of view.
   b) Erosion and dilation to remove "speckle" artifacts.
   c) Watershed transformation for "de-clumping" cells that were effectively touching.
   d) Drawing a line where two cell membranes met.

3. Feature Extraction

   Once cells were segmented, they were assigned unique labels (Object 1, Object 2, etc.). The following geometric properties were calculated for each labeled object:
   A. Area (A)
   The total number of pixels contained within the cell boundary, converted to square micrometers (μm2) using the microscope's metadata scale.
   B. Aspect Ratio (AR)
   The elongation of the cell, calculated by fitting an ellipse to the cell shape.

$$AR = \frac{MajorAxis}{MinorAxis}$$

Interpretation: An AR of 1.0 indicates a perfect circle; higher values indicate an elongated or spindle-like shape.

C. Circularity (C)

The closeness of the shape to a perfect circle, sensitive to both overall shape and boundary roughness.

$$C = 4\pi\ x \frac{Area}{Perimeter^2}$$

Using the algorithms, seen in Table 2, for quantitative morphological analysis of confocal microscope images, the mean and standard deviation for these parameters were collected for each disc per group ($N = 18$ discs/group) for statistical analysis and scoring, and a confocal morphology composite score was derived from a weighted combination of these fundamental parameters (area, aspect ratio, circularity) using a semi-quantitative grading system where morphology was assigned a numerical value (e.g., 1 for poor spreading, 5 for excellent

Table 2 Algorithms used for quantitative morphological analysis of confocal microscope images

Metric	Formula	Sensitivity
Area	$\sum Pixels$	Overall size/growth
Aspect Ratio	Maj/ Min	Polarization/Elongation
Circularity	$4\,\pi A/P^2$	Surface irregularity/Roundness

spreading) by a blinded evaluator. The higher confocal morphology scores indicated better morphology.

SEM of cell morphology

Cell morphology on the surfaces of the titanium discs in each group was further investigated using SEM (Phillips, JAPAN) on days 3 and 7. The samples were fixed for 12 h in 2.5% glutaraldehyde in 0.1 M cacodylate buffer at 4 °C, then dehydrated using an ethanol series of 30%, 50%, 75%, 90%, and 100% for 10 min at each concentration. Finally, the samples were vacuum dried, sputter-coated with gold, and imaged using SEM, in which more than 10 fields were examined per disc. SEM imaging was performed under high-vacuum mode at an accelerating voltage of 5 kV, with a working distance of approximately 32 mm. Images were acquired at a magnification of ×1,000. Secondary electron imaging mode was used to enhance topographical contrast. Brightness and contrast settings were kept constant across all groups. All imaging parameters were maintained consistently across samples to allow for reliable comparison.

Quantitative real-time PCR (qPCR)

The alkaline phosphatase (ALP) activity was analyzed to evaluate the osteogenic potential of the cells seeded on six discs from each group on days 3 and 7. The cultured immortalized human mesenchymal stem cells were washed twice with100 µL of calcium- and magnesium-free phosphate-buffered saline (PBS) containing 0.1% Triton (Triton X-100) to lyse the cells and fixed with 4% paraformaldehyde for 1 to 2 min at room temperature to preserve enzymatic activity. Then the cells were incubated in 200 µL ALP staining solution containing 10 mM of p-nitrophenol phosphate and 100 µL of 1.5 M of 2-amino-2-methyl-1-propanol buffer (Lab Assay ATP; Wako Pure Chemicals, Commonwealth of Virginia, USA) and incubated for 60 min at 60 °C. The colorimetric reaction was monitored microscopically and terminated upon optimal color development by washing the wells thoroughly with deionized water. Cells were subsequently counterstained with Hematoxylin / Nuclear Fast Red for 2 min and washed with water. The stained cells were kept hydrated in water and imaged using a brightfield microscope to identify ALP-positive cells exhibiting dense, granular cytoplasmic precipitates. The ALP activity was then measured as arbitrary units (au) using a spectrophotometer (Synergy HT; BioTek Instruments, Vermont, USA) at an absorbance rate of 405 nm.

For gene expression analysis, primer sequences for target genes are listed in (Table 3). Early osteogenic marker Runx2 expression was evaluated on day 3; intermediate markers osteopontin (OPN) and bone sialoprotein (BSP) on day 7; and late markers OPN (day 14) and osteocalcin (OCN, day 21). At each time point (days 3, 7, 14, and 21), total RNA was extracted using an RNA isolation kit with on-column DNase treatment to eliminate genomic DNA contamination. Reverse transcription was performed using 0.5–1.0 µg of total RNA per reaction to synthesize cDNA. Quantitative PCR (qPCR) was carried out using a QuantStudio™ 3 Real-Time PCR System (Applied Biosystems, USA). Each reaction was performed in a 20 µL total volume, and all samples were analyzed in technical triplicates. Gene expression levels were normalized to housekeeping genes (GAPDH and ACTB). Relative gene expression was calculated using the 2^−ΔΔCt method, where ΔCt = Ct(target gene) − Ct(reference gene), and ΔΔCt = ΔCt(sample) − ΔCt(calibrator). The calibrator was defined as Group I at the earliest time point, and results were expressed as fold changes relative to this baseline condition.

Table 3 Primer sequences used for quantitative real-time PCR (qPCR)

Gene	Forward Primer (5′→3′)	Reverse Primer (5′→3′)
Runx2 (Runt-related transcription factor 2)	CCA CTC TGC CTT CTC TCA CT	TGC CTC TGT CTT TGC TGT CT
ALP (Alkaline phosphatase)	CCT TCA CTC CTT ACT TGC TG	GAG TGG TGC TTT GGT CAT TG
BSP (Bone sialoprotein)	CAG AGG AGG CAA GCG TCA TA	GGA TTT GAG TGA GGT CCT GGA
OCN (Osteocalcin)	CTC ACA CTC CTC GCC CTA TT	GGC TCC CAG CCA TGT TTA

Statistical analysis

All statistical analyses were performed using R (Version 2025.09.2 for Mac; R Foundation for Statistical Computing, Vienna, Austria). Quantitative data are presented as mean and standard deviation (SD. The normality was assessed using the Shapiro–Wilk test, and the homogeneity of variances was evaluated using Levene's test. Inter-group comparisons were performed using one-way analysis of variance (ANOVA), followed by Tukey's honestly significant difference (HSD) post-hoc test for pairwise comparisons. The relationship between surface carbon content and alkaline phosphatase activity was examined using Pearson's correlation coefficient, with the coefficient of determination (r^2) to determine the proportion of explained variance. The threshold for statistical significance was set at $p < 0.05$.

Results

Surface characteristics

Surface roughness

Atomic force microscopy analysis demonstrated no statistically significant differences in surface roughness parameters (Ra and Rq) following UV photofunctionalization

across all four groups ($p < 0.05$) with Mean Ra values ranged from 369 to 377 nm, and mean Rq values from 448 to 459 nm (Table 4). The preserved nanoscale topography is illustrated in Fig. 4, confirm that UV irradiation modifies does not alter the underlying micro- and nano-topographical features generated by sandblasting and acid etching.

Table 4 Statistical summary of surface roughness parameters Ra and Rq across study groups

Roughness	Group	Mean	SD	F
Ra-Roughness	Group I	377.47	13.8	$F = 1.52, p = 0.223$
	Group II	371.66	17.9	
	Group III	369.12	10.5	
	Group IV	371.27	13.7	
Rq-Roughness	Group I	458.94	17.6	$F = 1.79, p = 0.163$
	Group II	452.18	14.7	
	Group III	448.19	11.0	
	Group IV	449.72	20.3	

F For one-way ANOVA, * significant at $p < 0.05$

Surface carbon content (EDS analysis)

Energy-dispersive X-ray spectroscopy (EDS) showed peaks for carbon, oxygen, aluminum, vanadium, and titanium across all groups (Fig. 5). EDS revealed a statistically significant reduction in surface carbon atomic percentage following UV photofunctionalization ($p < 0.001$; Table 5). The conventional UV protocol (Group II) has less hydrocarbon than the control group (Group I), whereas both VUV protocols (Groups III and IV) achieved greater hydrocarbon removal, with no statistically significant difference between Group III and IV. In contrast, the weight percentages of titanium (~87–89%), aluminum (~6%), and vanadium (~4%) remained unchanged across all groups, confirming that UV exposure selectively eliminated surface hydrocarbon contaminants without altering the bulk alloy composition.

Surface phases (XRD analysis)

X-ray diffraction (XRD) analysis corroborated the chemical changes observed at the Ti–6Al–4 V surface. In addition to the characteristic α-Ti and β-Ti reflections, a broad signal corresponding to amorphous carbon contamination was evident around 20–25° 2θ in the untreated control. The relative intensity of this carbon-associated signal diminished progressively across the treated groups, while the intensity of the TiO_2 reflections (anatase at ~25° 2θ and rutile at ~27–36° 2θ) increased correspondingly (Fig. 6). Semi-quantitative analysis of normalized peak intensities confirmed a highly significant inter-group difference, with the most pronounced reduction in carbon signal observed in the VUV-treated groups ($p < 0.001$; Table 6).

Time-of-flight secondary ion mass spectrometry (TOF-SIMS)

TOF-SIMS analysis provided surface-sensitive confirmation of the carbon reduction (Fig. 7). The control group showed a strong hydrocarbon-related

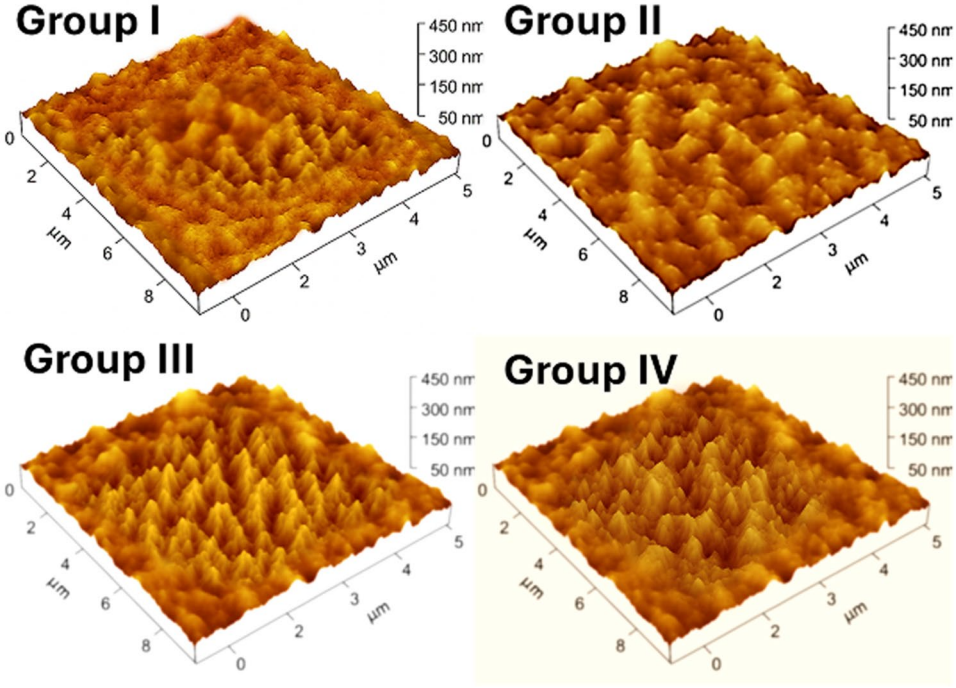


Fig. 4 Atomic force microscopy (AFM) analysis of surface roughness across study groups. **A** Representative AFM topographical images showing the similarity of surface morphology before and after UV exposure

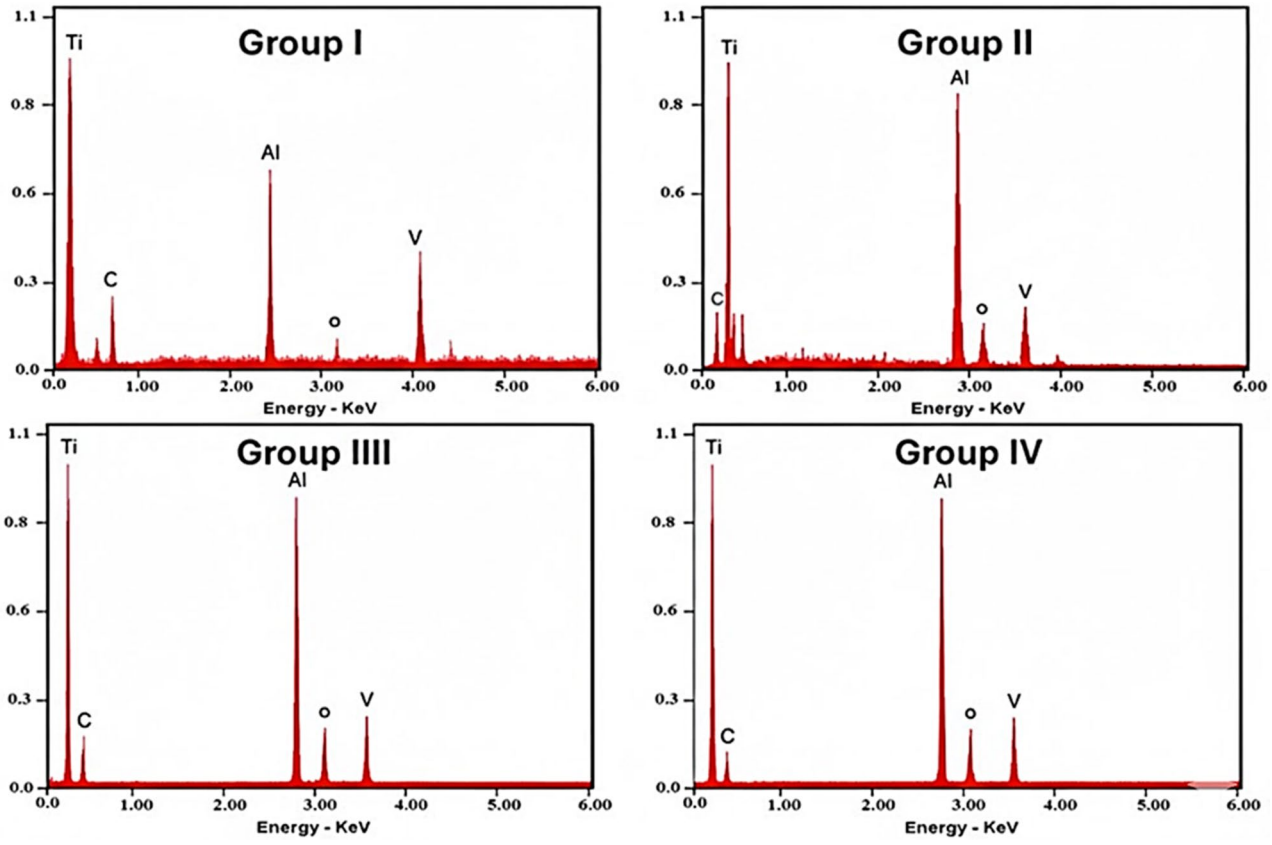


Fig. 5 Energy-dispersive X-ray spectroscopy (EDS) analysis of Ti–6Al–4 V across Groups I–IV. EDS spectra showing characteristic peaks for Carbon (C), Oxygen (O), Aluminum (Al), Vanadium (V), and Titanium (Ti); apparent peak shifts reflect variations in surface contamination rather than changes in alloy composition, with mean peak intensities normalized to controls via semi-quantitative analysis. (B) Boxplot of surface carbon atomic percentage across groups

Table 5 Atomic and weight percentages of surface carbon determined via energy-dispersive X-ray spectroscopy (EDS)

EDS	Mean ± SD	Group II	Group III	Group IV	F
Group I (N1 = 20)	21.44% ± 1.28%	$P < 0.001$*	$P < 0.001$*	$P < 0.001$*	F = 746, $p < 0.001$*
Group II (N2 = 20)	15.04 ± 1.56%		$P < 0.001$*	$P < 0.001$*	
Group III (N3 = 20)	8.98%± 0.711%			$p = 0.629$	
Group IV (N4 = 20)	8.57% ± 0.578%				

F for ANOVA and Tukey's post hoc test for pairwise comparison

*: significant at $p < 0.05$

signal corresponding to C^+ fragments at m/z 12–15, which decreased across the treated groups, with the most pronounced reductions observed in Groups III and IV ($p < 0.001$; Table 7). In contrast, oxygen- and titanium-related signals (O^-/OH^- at m/z 16–17; Ti^+ at m/z 51; TiO^+ at m/z 67) remained stable across all groups, confirming that UV exposure selectively reduced hydrocarbon contamination without altering the metallic alloy constituents.

Wettability

Contact angle measurements revealed a marked improvement in surface wettability following UV photofunctionalization (Fig. 8). The untreated control exhibited a moderately hydrophilic surface dominated by adsorbed hydrocarbons (76.9° ± 2.58°), while progressive treatment with conventional UV and VUV protocols produced transition toward a strongly hydrophilic state. The lowest contact angles were recorded in the VUV-treated groups (26.9° ± 1.04°). These differences were statistically significant ($p < 0.001$), with each treated group showing improved wettability compared with the control group (Table 8).

Cell culture results

MTT assays

Cell viability (MTT) assays revealed markedly higher metabolic activity in BM-MSC/TERT292 cells grown on the treated groups compared with the control, reflecting enhanced proliferation on surfaces where carbon contamination had been minimized. Quantitatively, absorbance values increased stepwise across the treatment

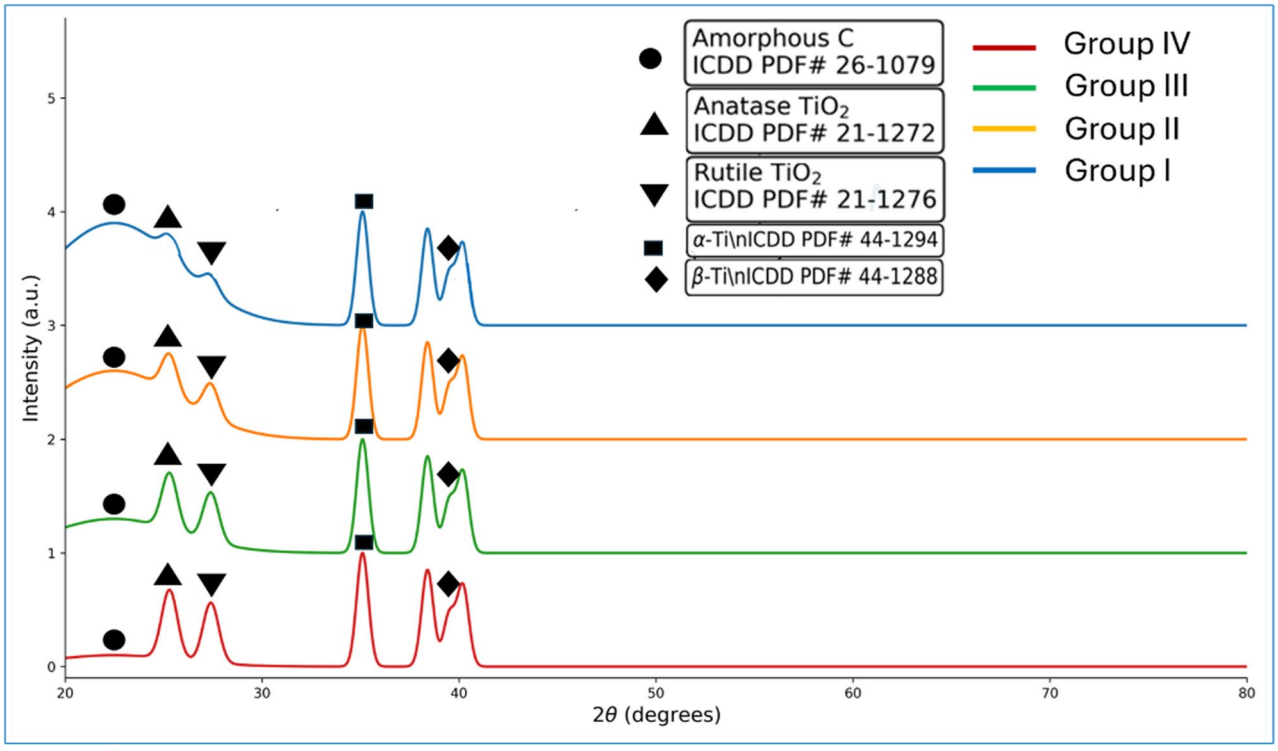


Fig. 6 X-ray diffraction (XRD) analysis of Ti–6Al–4 V across groups. Diffraction patterns illustrating the diminishing broad carbon peak (20–25° 2θ) with UV treatment alongside increasing TiO_2 peaks (anatase ~ 25°; rutile ~ 27–36°)

Table 6 Semiquantitative analysis of amorphous carbon peak intensity (XRD), arbitrary units

XRD	Mean ± SD	Group II	Group III	Group IV	F
Group I (N1 = 20)	94.6 ± 2.73	$P < 0.001$*	$P < 0.001$*	$P < 0.001$*	F = 6158, $p < 0.001$*
Group II (N2 = 20)	64.3 ± 2.70		$P < 0.001$*	$P < 0.001$*	
Group III (N3 = 20)	34.9 ± 2.52			$P < 0.001$*	
Group IV (N4 = 20)	10.1 ± 1.3				

F for ANOVA and Tukey's post hoc test for pairwise comparison

*: significant at $p < 0.05$

sequence, with one-way ANOVA confirming significant intergroup differences ($p < 0.001$) (Table 9).

Laser confocal microscopy imaging

Laser confocal microscopy imaging of BM-MSC/TERT292 cytoskeletal organization (Fig. 9) further substantiated these findings. In the untreated controls, cells appeared sparsely distributed with rounded morphologies and poor spreading, consistent with a hydrophobic, carbon-rich surface. In contrast, the treated discs exhibited confluent layers of elongated, well-spread osteoblast-like cells, with clear actin filaments and nuclei alignment (Table 10).

Alkaline phosphatase (ALP) activity

Alkaline phosphatase (ALP) activity assays showed markedly higher enzymatic activity in cells cultured on surfaces of Groups II, III, and IV as compared with Group I (Fig. 10). The ALP signal increased proportionally with the degree of carbon reduction, and statistical analysis confirmed a strong group effect ($p < 0.001$) (Table 11).

To verify the relationship between hydrocarbon removal and osteogenic activation, Pearson correlation analyses were performed between per-disc ALP activity and the corresponding carbon content for each of the three analytical techniques ($n = 72$ paired specimens). A strong inverse correlation was confirmed for all three techniques (EDS: $r = -0.886$, XRD: $r = -0.876$,; TOF-SIMS: $r = -0.885$, all $p < 0.001$) with about 77–79% of the variance in ALP activity was explained by surface carbon content (Fig. 11).

SEM imaging

On Group I discs, SEM revealed isolated BM-MSC/TERT292 cells, with limited filopodia extension, whereas UV-treated Groups II, III, and IV showed dense cellular coverage with extensive filopodia bridging across surface features, forming interconnected cellular networks and extracellular matrix deposition (Fig. 12).

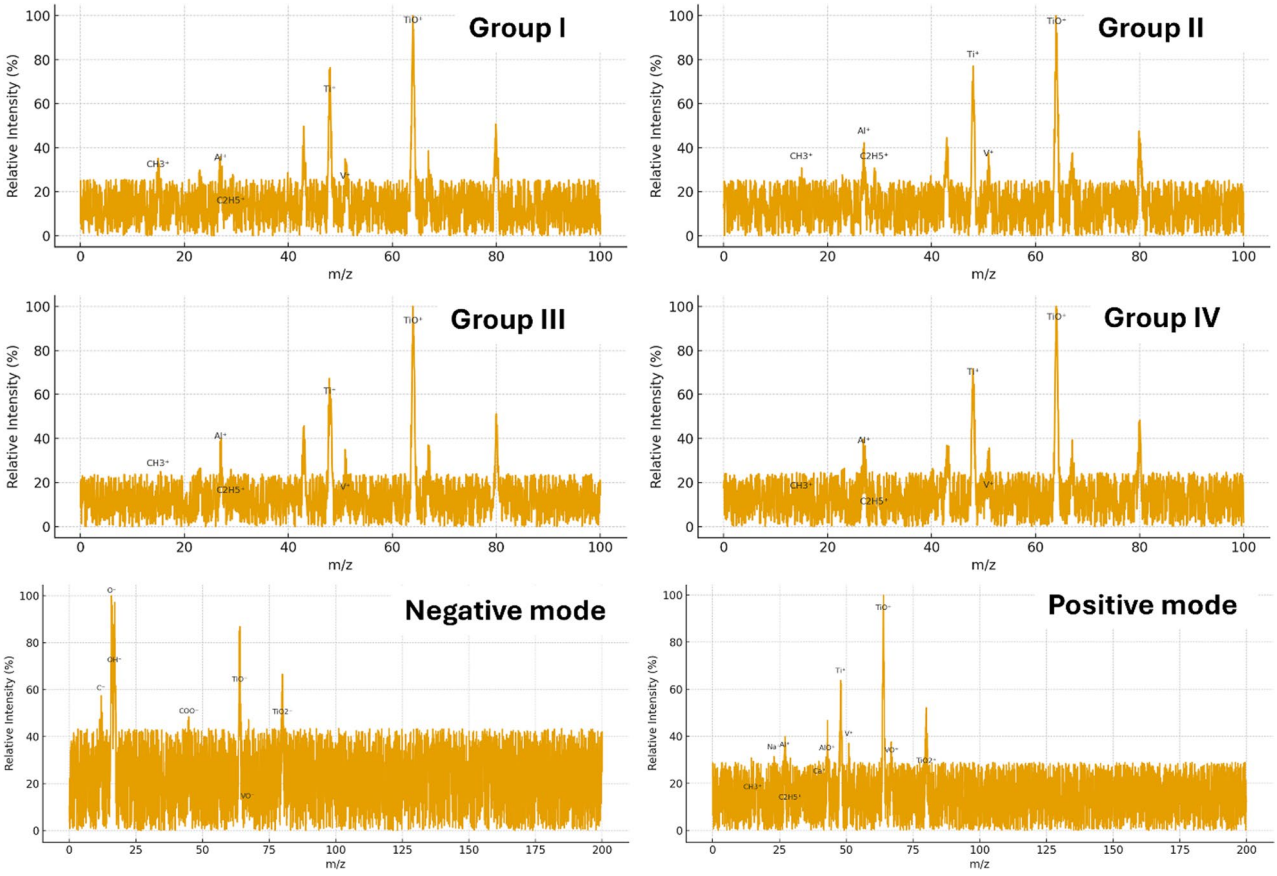


Fig. 7 Time-of-Flight Secondary Ion Mass Spectrometry (TOF-SIMS) analysis of Ti–6Al–4 V across groups. Mass spectra showing a strong carbon-related signal (C^+ fragments, m/z ~ 12–15) in Group I that progressively decreased with UV exposure (Groups II–IV), while oxygen/hydroxyl fragments (m/z ~ 16–17) and titanium-related fragments (m/z ~ 51, 67) remained stable

Table 7 Normalized intensity of surface carbon signal determined with TOF-SIMS arbitrary units analysis

TOF-SIMS	Mean ± SD	Group II	Group III	Group IV	F
Group I (N1 = 20)	93.6 ± 2.95	$P < 0.001$*	$P < 0.001$*	$P < 0.001$*	F = 1390, $p < 0.001$*
Group II (N2 = 20)	66.9 ± 5.04		$P < 0.001$*	$P < 0.001$*	
Group III (N3 = 20)	33.6 ± 4.95			$P < 0.001$*	
Group IV (N4 = 20)	24.9 ± 4.46				

F for ANOVA and Tukey's post hoc test for pairwise comparison

*: significant at $p < 0.05$

Gene expression of the cells analyzed using real-time quantitative polymerase chain reaction (qPCR)

As seen in Fig. 12, gene expression analysis further confirmed the osteogenic commitment of BM-MSC/TERT292 cells in response to reduced carbon surface. On day 3, early osteogenic marker Runx2 was expressed at baseline in the control group (Group I) that was used as a calibrator, whereas UV-treated groups showed higher levels. Group II demonstrated a modest but significant increase compared with the control (*$p < 0.05$), while Groups III and IV exhibited further upregulation ($p < 0.001$ vs. control), without a statistically significant difference between them ($p > 0.05$). By day 7, bone sialoprotein (BSP) expression followed the same pattern, with Group II moderately elevated (*$p < 0.05$ vs. control) and Groups III and IV significantly higher than the control ($p < 0.001$) yet not different from each other ($p > 0.05$). On day 14, the late osteogenic differentiation marker OPN expression was similar to day 7 but with higher values ($p < 0.001$). Finally, On day 21, OCN expression followed the same pattern as the earlier markers: Group II was significantly higher than Group I ($p < 0.05$), and both Group III and Group IV were significantly higher than Group II ($p < 0.01$). However, no statistically significant difference was observed between Group III and Group IV ($p > 0.05$). (Fig. 13) (Table 12).

Discussion

The shift from minutes-long UV activation to second-scale VUV treatment represents a major technological transition in implant surface science. The present study compared the physicochemical and biological effects of conventional UV and VUV photofunctionalization

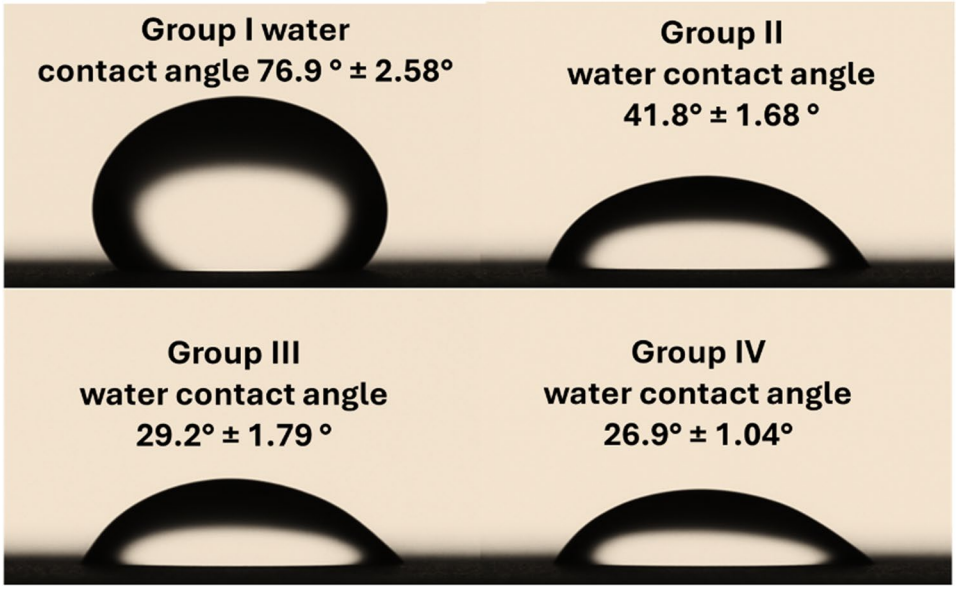


Fig. 8 Surface wettability of Ti–6Al–4 V across groups representative goniometer images of static water contact angles on the titanium surface

Table 8 Surface wettability of Ti–6Al–4V across groupsRepresentative goniometer images of static water contact angles on the titanium surface

Contact	Mean ± SD	Group II	Group III	Group IV	F
Group I (N1 = 20)	76.9° ± 2.58 °	$P < 0.001$*	$P < 0.001$*	$P < 0.001$*	F = 2256, $p < 0.001$*
Group II (N2 = 20)	41.8 ° ± 1.68 °		$P < 0.001$*	$P < 0.001$*	
Group III (N3 = 20)	29.2 ° ± 1.79 °			$P < 0.001$*	
Group IV (N4 = 20)	26.9 ° ± 1.04 °				

F for ANOVA and Tukey's post hoc test for pairwise comparison

*: significant at $p < 0.05$

Table 9 Analysis of (BM-MSC/TERT292) cell viability with MTT assay

MTT	Mean ± SD	Group II	Group III	Group IV	F
Group I (N1 = 18)	0.51 ± 0.08	$P < 0.001$*	$P < 0.001$*	$P < 0.001$*	F = 71, $p < 0.001$*
Group II (N2 = 18)	0.79 ± 0.12		$P = 0.004$*	$P < 0.001$*	
Group III (N3 = 18)	0.95 ± 0.13			$P = 0.966$	
Group IV (N4 = 18)	0.97 ± 0.18				

F for ANOVA and Tukey's post hoc test for pairwise comparison

*: significant at $p < 0.05$

on sandblasted, acid-etched grade V titanium alloy (Ti6Al4V). Our findings demonstrated that both approaches effectively rejuvenated the titanium surfaces by removing hydrocarbon contaminants, improving surface wettability, and subsequently enhancing osteogenic responses in vitro. Importantly, the tested VUV device achieved these outcomes in only 20 s, compared with the 12–15 min required by the conventional UV devices examined, highlighting significant translational advantages for clinical use. The core finding is the time efficiency of VUV, with the DIO UV Activator (20 s) achieving results equivalent to the TheraBeam Affiny (15 min) and better than the conventional TheraBeam Super Osseo (12 min). The capability of the 20-second protocol is driven by the high photon energy of the 172 nm wavelength, which enables the direct dissociation of organic chemical bonds and the rapid generation of reactive oxygen species. This dual mechanism bypasses the slower photocatalytic dependence of conventional UV, achieving equivalent hydrocarbon removal and biological activation in a fraction of the time.

An important methodological variable in the present study is the marked difference in exposure times between conventional UV and VUV photofunctionalization protocols, which may have influenced both the physicochemical and biological outcomes. While longer exposure durations in conventional UV systems (12–15 min) allow for gradual photocatalytic decomposition of hydrocarbons, the significantly shorter exposure time of the VUV protocol (20 s) relies on higher photon energy to induce rapid photochemical reactions. This distinction suggests that treatment efficacy is not solely time-dependent but rather governed by the interplay between irradiation time and photon energy. In the current findings, despite the substantial reduction in exposure duration, VUV treatment achieved equal or superior hydrocarbon removal, wettability enhancement, and osteogenic responses compared with conventional UV, indicating a more efficient activation mechanism. However, it is also possible that

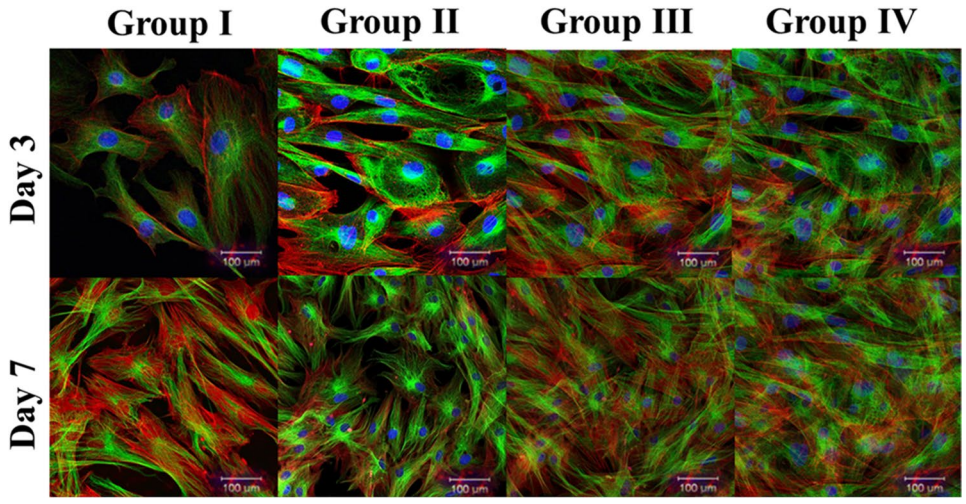


Fig. 9 Confocal microscopy analysis of BM-MSC/TERT292 cell morphology on treated titanium surfaces across groups. Representative immunofluorescence confocal images illustrating cell morphology and distribution

Table 10 Confocal morphology composite score: quantitative morphological analysis of BM-MSC/TERT292 cell morphological parameters

Confocal	Mean ± SD	Group II	Group III	Group IV	F
Group I (N1 = 18)	0.45 ± 0.12	$P < 0.001$*	$P < 0.001$*	$P < 0.001$*	F = 71, $p < 0.001$*
Group II (N2 = 18)	0.73 ± 0.10		$P < 0.001$*	$P < 0.001$*	
Group III (N3 = 18)	0.91 ± 0.13			$P = 0.943$	
Group IV (N4 = 18)	0.93 ± 0.08				

F for ANOVA and Tukey's post hoc test for pairwise comparison

*: significant at $p < 0.05$

Table 11 Analysis of Day 3 And 7 Average ALP activity across study groups

ALP	Mean ± SD	Group II	Group III	Group IV	F
Group I (N1 = 18)	0.39 ± 0.09	$P < 0.001$*	$P < 0.001$*	$P < 0.001$*	F = 71, $p < 0.001$*
Group II (N2 = 18)	0.65 ± 0.09		$P < 0.001$*	$P < 0.001$*	
Group III (N3 = 18)	0.88 ± 0.12			$P = 0.718$	
Group IV (N4 = 18)	0.91 ± 0.08				

F for ANOVA and Tukey's post hoc test for pairwise comparison

*: significant at $p < 0.05$

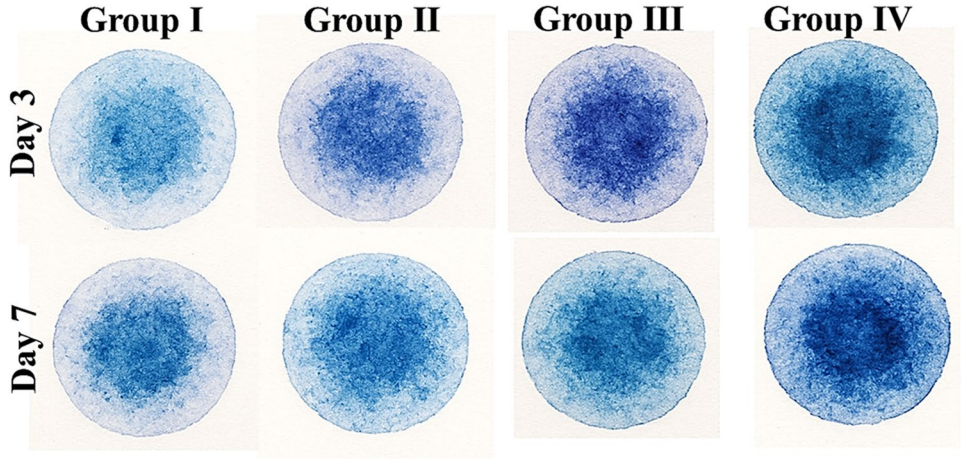


Fig. 10 Alkaline Phosphatase (ALP) activity of BM-MSC/TERT292 cells on treated titanium surfaces. Representative ALP staining images across groups at days 3 and 7 across groups

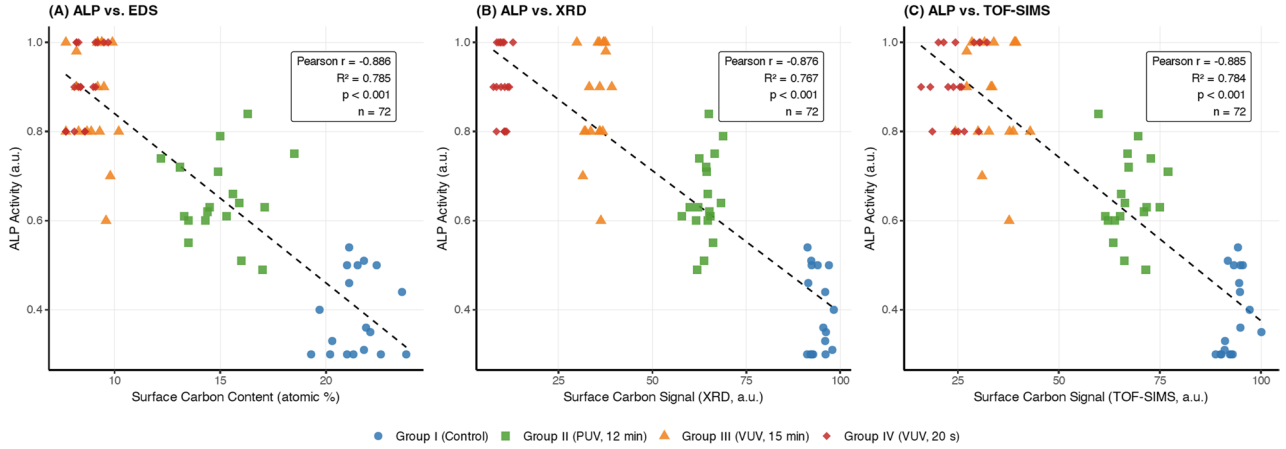


Fig. 11 Per-disc Pearson correlation between Alkaline Phosphatase (ALP) activity and surface carbon content as measured by three independent analytical techniques: (**A**) Energy-dispersive X-ray Spectroscopy (EDS), (**B**) X-ray Diffraction (XRD), and (**C**) Time-of-Flight Secondary Ion Mass Spectrometry (TOF-SIMS)

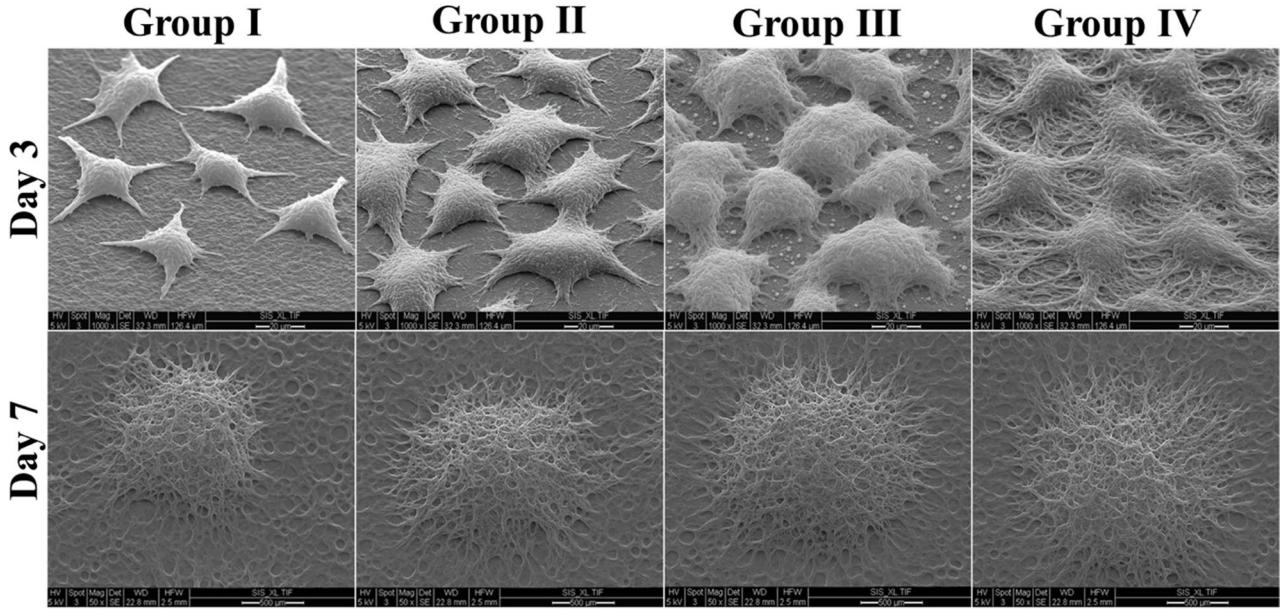


Fig. 12 Scanning electron microscope images of cells cultured on days 3 and 7 across groups

prolonged exposure in conventional systems may reach a plateau effect, beyond which no additional biological benefit is achieved, whereas high-energy VUV rapidly reaches this threshold. Therefore, the observed differences in outcomes should be interpreted as a function of energy dose (irradiance × time) rather than time alone. Future studies investigating standardized energy delivery across different UV systems would be valuable to further elucidate the relative contributions of exposure duration and photon energy to surface activation and subsequent cellular responses.

In agreement with prior reports, AFM analysis confirmed that UV irradiation did not alter the roughness of titanium surfaces. This aligns with findings by Rupp et al. [21], who emphasized that UV treatment influences surface chemistry without affecting the mechanical topography. Similarly, Li et al. [16] demonstrated that sandblasted/acid-etched topographies were preserved following UV exposure, reinforcing that the biological enhancements observed in the present study are attributable to chemical, rather than morphological alterations.

A major effect of UV treatment was the progressive reduction in surface carbon contamination, as confirmed via EDS, XRD, and TOF-SIMS analyses in this study. The untreated control discs in Group I showed a high carbon content (22.0 ± 1.3%), consistent with "biological aging" reported by Att and Ogawa [15] and Choi et al. [8], in which hydrocarbon pellicle accumulation decreased surface energy and impaired cellular interactions. Following UV exposure, surface carbon decreased

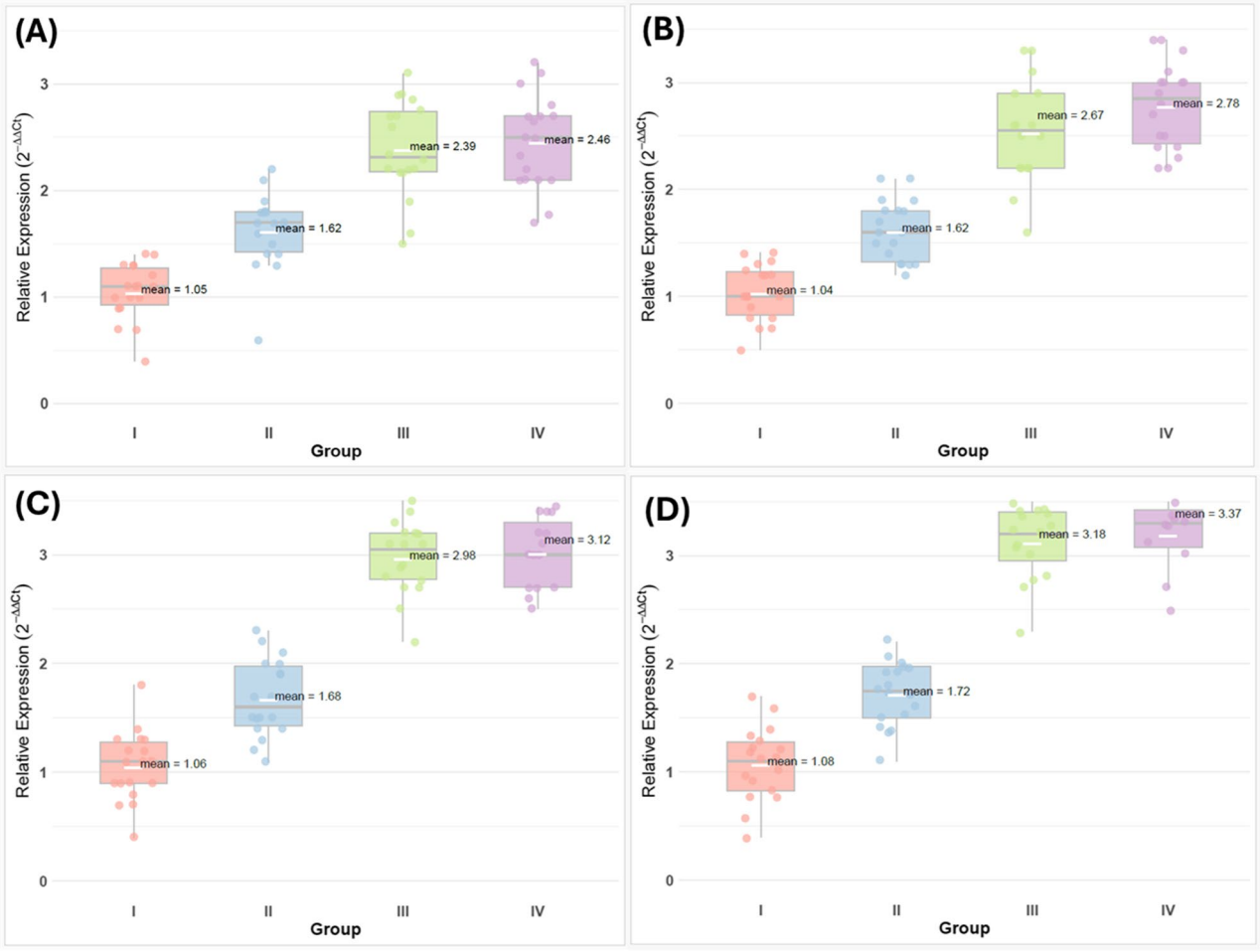


Fig. 13 Time-course analysis of relative osteogenic differentiation gene expression in BM-MSC/TERT292 cells: (**A**) day 3: Runx2; (**B**) day 7: BSP; (**C**) day 14: OPN; (**D**) day 21: OCN. Data are expressed as relative expression levels (2^−ΔΔCt), normalized to GAPDH/ACTB

significantly, reaching as low as 9% with the TheraBeam Affiny and 8% with the DIO UV Activator. These findings corroborate earlier TOF-SIMS investigations by Hierro-Oliva et al. [9], who demonstrated efficient hydrocarbon decomposition and enrichment of titanium oxide states following UV-C exposure. The reductions achieved using the 20-second VUV protocol highlight the enhanced efficiency of high-energy VUV photons in promoting rapid surface decontamination.

Moreover, the results of the current work imply that the treatments not only reduced surface carbon but also promoted the stabilization of crystalline titanium oxides, which are essential for bioactivity and osseointegration as the XRD revealed a concurrent increase in crystalline TiO_2 phases (anatase and rutile), consistent with the oxide surface stabilization reported by Barberi et al. [10, 11]. This oxide enrichment is important as TiO_2 is directly implicated in protein adsorption, cell adhesion, and osteoconduction. Collectively, these findings align with the observations of Suzumura et al. [13, 33], who demonstrated that VUV photons (172 nm) decompose organic molecules more efficiently than conventional UV wavelengths, yielding faster and more complete surface reactivation. The removal of hydrocarbons translated into improved wettability, as reflected by reduced contact angles (from 76.4° in controls to 27.0° after VUV). This transition towards a super-hydrophilic state is consistent with previous findings by Komatsu et al. [23], who reported that UV-modified titanium surfaces regain high surface energy, facilitating protein adsorption and integrin-mediated adhesion. Similarly, Henningsen et al. [17] demonstrated that both UV and plasma treatments significantly enhanced wettability, suggesting that the mechanism is primarily mediated by carbon decomposition rather than physical restructuring. The present study therefore confirms the strong linkage between surface chemistry, wettability, and subsequent biological performance. Enhanced cell proliferation observed in MTT assays was consistent with studies by Aita et al. [14] and Huang et al. [18], which demonstrated that osteoblasts exhibit improved viability and proliferation on UV-treated titanium. Confocal microscopy further

Table 12 Relative gene expression levels (2^−ΔΔCt) of osteogenic markers in BM-MSC/TERT292 cells for early (Runx2), intermediate (BSP), and late (OCN and OPN) osteogenic differentiation markers measured with qPCR on days 3, 7, 14, and 21

Runx2, _Day3	Mean ± SD	Group II	Group III	Group IV	F
Group I (N1 = 18)	1.05 ± 0.26	$P < 0.001$*	$P < 0.001$*	$P < 0.001$*	F = 56.4, $p < 0.001$*
Group II (N2 = 18)	1.63 ± 0.36		$P < 0.001$*	$P < 0.001$*	
Group III (N3 = 18)	2.39 ± 0.45			$P = 0.956$	
Group IV (N4 = 18)	2.46 ± 0.43				
BSP_Day7	**Mean ± SD**	**Group II**	**Group III**	**Group IV**	**F**
Group I (N1 = 18)	1.04 ± 0.27	$P < 0.001$*	$P < 0.001$*	$P < 0.001$*	F=94.3$P < 0.001$*
Group II (N2 = 18)	1.62 ± 0.29		$P < 0.001$*	$P < 0.001$*	
Group III (N3 = 18)	2.67 ± 0.6			$P = 0.848$	
Group IV (N4 = 18)	2.78 ± 0.34				
OPN_Day14	**Mean ± SD**	**Group II**	**Group III**	**Group IV**	**F**
Group I (N1 = 18)	1.06 ± 0.32	$P < 0.001$*	$P < 0.001$*	$P < 0.001$*	F = 56.4, $p < 0.001$*
Group II (N2 = 18)	1.68 ± 0.35		$P < 0.001$*	$P < 0.001$*	
Group III (N3 = 18)	2.98 ± 0.33			$P = 0.956$	
Group IV (N4 = 18)	3.12 ± 0.36				
OCN_Day21	**Mean ± SD**	**Group II**	**Group III**	**Group IV**	**F**
Group I (N1 = 18)	1.08 ± 0.33	$P < 0.001$*	$P < 0.001$*	$P < 0.001$*	F = 188, $p < 0.001$*
Group II (N2 = 18)	1.72 ± 0.3		$P < 0.001$*	$P < 0.001$*	
Group III (N3 = 18)	3.18 ± 0.35			$P = 0.334$	
Group IV (N4 = 18)	3.37 ± 0.36				

F for ANOVA and Tukey's post hoc test for pairwise comparison

*: significant at $p < 0.05$

revealed improved cytoskeletal organization, with cells exhibiting elongated morphologies and aligned actin filaments on UV-treated surfaces. These observations align with those of Yin et al. [19], who reported that BM-MSCs show enhanced osteogenic expression on UV-treated 3D-printed Ti6Al4V. SEM observations confirmed extensive filopodia extensions and extracellular matrix deposition on UV-treated surfaces, indicative of enhanced integrin-mediated adhesion. Such morphological characteristics are essential for establishing stable cell–substrate interactions and have been linked to early stages of osseointegration in vivo, as reported by Mehl et al. [23] and Chang et al. [31]. These findings highlight the importance of UV surface treatment to promote rapid bone–implant integration. ALP activity, an established marker of early osteogenesis, increased significantly with UV treatment, particularly in Groups III and IV. This observation aligns with the findings of Choi et al. [7, 8], who demonstrated that ALP expression is closely linked to surface hydrophilicity. Gene expression assays further confirmed the enhanced osteogenic commitment, with Runx2, BSP, OPN, and OCN all significantly upregulated. These findings mirror previous reports by Li et al. [16] and Yamuna et al. [3], which demonstrated elevated osteogenic marker expression following UV exposure.

Interestingly, while both the TheraBeam Affiny (15 min VUV) and DIO UV Activator (20 s VUV) achieved similar biological outcomes, their required exposure times differed greatly. This highlights the efficiency of high-energy VUV in driving rapid surface activation, in line with the observations of Suzumura et al. [13] and Matsuura et al. [2]. From a translational standpoint, the

reduced activation time of VUV devices represents a major advancement. The DIO UV Activator, requiring only 20 s, achieved equivalent biological responses to devices requiring 12–15 min. This is consistent with the paradigm shift described by Matsuura et al. [2], which emphasized energy and speed as critical determinants in implant surface activation. The ability to perform chairside activation within seconds enhances clinical feasibility and patient workflow, reducing procedural delays. Moreover, previous clinical reports, such as that of Cardarelli [34], have demonstrated accelerate osseointegration following UV activation, supporting the translational potential of the current findings.

The remarkable finding is that an ultra-rapid 20-second vacuum-ultraviolet (VUV) irradiation protocol (Group IV) provides identical surface cleaning and biological bioactivity to a prolonged 15-minute VUV protocol (Group III) warrants a deeper mechanistic exploration. Photochemically, the 172 nm VUV light generated by the xenon excimer lamp emits photons with an energy of approximately 7.2 eV. This energy level directly exceeds the bond dissociation energies of common organic covalent bonds typical of aging-induced hydrocarbon contamination, such as C–C (~ 3.6 eV) and C–H (~ 4.3 eV). Consequently, VUV irradiation drives direct photolysis and cleavage of organic molecules independently of the classic, slower titanium-dioxide-mediated photocatalysis relied upon by conventional UV light (~ 250–360 nm). Furthermore, 172 nm light is heavily absorbed by ambient oxygen, yielding high-density reactive oxygen species, including ozone (O_3) and atomic oxygen (O (^{1}D)), which rapidly volatilize the cleaved hydrocarbons into CO_2 and H_2O. To explain the equivalence observed between the 20-second and 15-minute VUV protocols, we propose a 'surface-cleaning plateau hypothesis.' We hypothesize that hydrocarbon removal and the subsequent transition to a super hydrophilic state are self-limiting surface phenomena; once the outermost adsorbed hydrocarbon layers are completely volatilized and the surface hydroxyl (OH^-) density reaches its absolute saturation threshold, additional VUV exposure cannot further lower the contact angle or alter the crystalline oxide phases. This phenomenon is strongly supported by analogue studies by Suzumura et al. [32] and Matsuura et al. [2], who similarly noted that high-energy VUV photons rapidly drive surface reactions to a functional plateau, rendering extended exposure times redundant for clinical bioactivity. The variation between the two VUV devices tested in this study likely stems from distinct engineering configurations, such as differences in lamp power/irradiance, source-to-sample proximity, or optimized atmospheric control within the compact chairside chamber of the 20-second device, which maximizes the localized flux of reactive species.

When comparing our outcomes with broader literature, several coherent and distinct aspects emerge. Coherent with the foundational work of Att and Ogawa [15], our data demonstrate a clear, inverse correlation between surface carbon content and osteogenic cellular response, reinforcing that the elimination of biological aging is mandatory to unlock the full osseointegrative potential of titanium. Likewise, our finding that surface roughness parameters (Ra and Rq) remain unaltered across all treatment groups aligns perfectly with analogue studies by Rupp et al. [21] and Li et al. [16], confirming that UV photofunctionalization is strictly a surface-chemistry modification that preserves underlying macro- and micro-topographies.

Conversely, a major distinct aspect of the present study lies in our substrate choice and comprehensive analytical methodology. While many historical analogue studies utilized polished or pure titanium (Grade IV) disks, our study evaluated a clinically representative Grade V titanium alloy (Ti6Al4V) exhibiting a complex sandblasted and dual-acid-etched (SLA) topography that underwent a controlled, 4-week aging process. By corroborating our surface findings across three separate analytical pathways-quantitative EDS, semi-quantitative crystalline phase evaluation via XRD, and trace molecular detection via TOF-SIMS-we have demonstrated that a 20-second ultra-rapid protocol successfully penetrates and rejuvenates complex, clinically relevant microtopographies. This provides strong mechanistic assurance that the rapid chairside workflow can be translated to commercial dental implant geometries without sacrificing biological efficacy.

In conclusion, this work confirms that UV photofunctionalization rejuvenates titanium surfaces by removing hydrocarbons, enhancing wettability, and promoting osteogenic responses. Both conventional and VUV devices were effective; however, VUV demonstrated superior efficiency, achieving equivalent biological benefits in seconds rather than minutes. These findings position VUV photofunctionalization as a promising and clinically applicable strategy to overcome hydrocarbon surface contamination of titanium implants and accelerate early osseointegration.

The present study had several limitations. First, the present study was limited to in vitro assays. This study used the hTERT-MSC cell line (immortalized cells), which might exhibit altered phenotypes and different behavior from primary human mesenchymal stem cells (hMSCs). While hTERT-MSCs provide reproducibility and reduced donor variability, they may exhibit altered proliferation rates and differentiation kinetics compared to primary hMSCs, potentially leading to enhanced osteogenic responsiveness. Therefore, the magnitude of biological effects observed in this study may differ from

primary cell behavior [1–3, 40, 42]. Second, a freshly prepared SLA surface could serve as an additional reference point to determine whether UV treatment restores or enhances the original surface state. Based on existing literature, photofunctionalization primarily restores surface energy lost through aging, although some studies suggest it may transiently enhance bioactivity beyond baseline levels as the photophysicochemical excitation by 172 nm photons frequently drives the titanium dioxide layer into a temporary "superhydrophilic" state that can exceed the base free energy levels of merely freshly processed, un-irradiated titanium [7]. Third, the 10 × 10 μm^2 AFM scan captures nanoscale roughness; however, SLA surfaces exhibit hierarchical micro- and macro-topography. Therefore, AFM results should be interpreted as representative of nanoscale features only. Moreover, although Ra and Rq provide standard amplitude-based descriptors of nanoscale roughness, they do not capture the symmetry or peakedness of the surface height distribution. Higher-order statistical parameters such as skewness and kurtosis, as well as multi-scale characterization using profilometry or larger-area AFM scans, would provide a more comprehensive description of the SLA topography and are recommended for future studies [12, 28, 33]. Fourth, static contact angles were used for standardization; dynamic measurements may provide additional insight and are recommended for future studies [9, 12, 26]. Finally, While the results provide strong mechanistic evidence, in vivo validation is necessary to confirm long-term osseointegration outcomes, bone-to-implant contact, and functional stability [14, 18, 19]. Animal and human clinical trials will be essential to determining the durability of UV-induced surface modifications under physiological loading. Additionally, cost-effectiveness analyses comparing conventional and VUV technologies should be explored to support broader clinical translation.

Conclusion

Within the limitations of this in vitro investigation, the present study provides comprehensive physicochemical and biological evidence that ultraviolet (UV) photofunctionalization effectively reverses the biological aging of Ti–6Al–4 V titanium surfaces. Both conventional UV and vacuum ultraviolet (VUV) irradiation significantly reduced surface hydrocarbon contamination, enhanced surface wettability, and promoted a cascade of favorable cellular responses, including increased proliferation, improved cytoskeletal organization, elevated alkaline phosphatase (ALP) activity, and upregulated expression of early, intermediate, and late osteogenic markers.

Importantly, these biological enhancements were achieved without altering the surface topography, confirming that the observed improvements are primarily driven by modifications in surface chemistry rather than morphological changes. The progressive reduction in carbon content, as demonstrated by EDS, XRD, and TOF-SIMS analyses, was strongly correlated with increased hydrophilicity and enhanced cellular bioactivity, highlighting the critical role of surface decontamination in optimizing implant–bone interactions.

A key finding of this study is the superior efficiency of VUV photofunctionalization. The 172 nm xenon excimer-based VUV devices (Groups III and IV) achieved significantly greater hydrocarbon removal and biological activation compared with conventional UV treatment, with the most notable advantage being the dramatic reduction in required exposure time. The DIO UV Activator, in particular, achieved surface activation within 20 s, producing physicochemical and biological outcomes comparable to those obtained with 12–15 min of conventional UV irradiation. This finding underscores the high photonic energy and enhanced photochemical reactivity of VUV, enabling rapid and effective surface rejuvenation.

From a translational and clinical perspective, this reduction in treatment time represents a substantial advancement. The ability to perform effective photofunctionalization in seconds facilitates seamless chairside integration, minimizes workflow disruption, and reduces the risk of surface recontamination prior to implant placement. Consequently, VUV technology addresses one of the primary limitations associated with conventional UV protocols and enhances the practicality of routine clinical implementation.

Collectively, the results of this study support the concept that surface chemical optimization—specifically hydrocarbon removal and restoration of surface energy—is a decisive factor in enhancing osteogenic potential. While both UV modalities are effective, VUV photofunctionalization offers a clear advantage in efficiency without compromising biological outcomes.

Future investigations should focus on in vivo validation, long-term osseointegration outcomes, and clinical trials to confirm the durability and translational impact of these findings. Additionally, cost-effectiveness analyses and comparisons across implant systems would further support the broader adoption of VUV technology in implant dentistry.

In summary, VUV photofunctionalization represents a rapid, efficient, and clinically feasible strategy for titanium surface activation, with the potential to significantly improve early implant integration and clinical success rates.

Abbreviations

ALP	Alkaline phosphatase
AFM	Atomic force microscopy
BSP	Bone sialoprotein
EDS	Energy-dispersive X-ray spectroscopy

Ti–6Al–4V	Grade V titanium alloy
BMSCs	Human bone marrow mesenchymal stem cells
Ra, arithmetical mean roughness, and Rq, root mean square roughness	Quantitative surface roughness parameters
Runt x2	Runx2
OCN	Osteocalcin
OPN	Osteopontin
qPCR	Quantitative polymerase chain reaction
TOF-SIMS	Time-of-flight secondary ion mass spectrometry
UV	Ultraviolet
VUV	Vacuum–UV
XRD	X-ray diffraction

Supplementary Information

The online version contains supplementary material available at https://doi.org/10.1186/s12903-026-08777-7.

Supplementary Material 1.

Acknowledgements
The researchers would like to thank the Deanship of Graduate Studies and Scientific Research at Qassim University (www.qu.edu.sa) for financial support (QU-APC-2026).

Authors' contributions
M.A.A., A.E., B.A.A., N.A., and R.A. prepared the samples and conducted the photofunctionalization. A.M.E. conducted the cell culture and its characterization. R.E. collected the results and performed the statistical analysis. All authors participated in writing and reviewing the manuscript.

Funding
This research received no external funding.

Data availability
All data generated or analyzed during this study are included in this published article.

Declarations

Ethics approval and consent to participate
Institutional Review Board Statement: This study received ethical approval from Qassim University Institutional Review Board (IRB # 24-01-32) in 23rd of January 2024. The research was conducted in full compliance with the ethical standards laid down in the 1964 Declaration of Helsinki and its later amendments. All procedures were performed in compliance with relevant laws and institutional guidelines and have been approved by the appropriate institutional committee(s).

Consent for publication
Not applicable.

Competing interests
The authors declare no competing interests.

Received: 1 February 2026 / Accepted: 25 May 2026
Published online: 18 July 2026

References

1. Park G, Komatsu K, Ogawa T. Optimizing implant osseointegration, soft tissue responses, and bacterial inhibition: a comprehensive narrative review on UV photofunctionalization of titanium. J Prosthodont Res. 2025;10:123–35.
2. Matsuura T, Komatsu K, Kido D, Ogawa T. The next frontier in osseointegration: energy and speed as critical determinants and their enhancement by UV photofunctionalization. J Mech Behav Biomed Mater. 2025;15:201–15.
3. Yamuna R, et al. Photofunctionalization of dental implants – a literature review. Int J Dent Stud. 2025;7:45–59.
4. Chacko N, Sukumaran K, Ravindran S, Karunakaran HK, Ravichandran R, Nair VV. Enhancing osseointegration: A comprehensive review of UV photofunctionalization for titanium dental implants. IP Annals Prosthodont Restor Dentistry. 2025;11:107–4.
5. Roy M, De Abreu PH, Etemadi N, Angelopoulos C. Positive effects of UV-photofunctionalization of titanium dental implants. J Funct Biomater. 2022;13(12):49–63.
6. Naauman Z, AlKheraif AA, Vohra F, et al. Ultraviolet A and C light-induced reduction of surface hydrocarbons on titanium implants. J Pharm Bioallied Sci. 2019;11(Suppl 2):S231–8.
7. Choi SH, Jeong WS, Cha JY, et al. Overcoming the biological aging of titanium using a wet storage method after ultraviolet treatment. Sci Rep. 2017;7:3833–45.
8. Choi SH, et al. Effect of ultraviolet light treatment and storage methods on biologic activity of titanium implants. Dent Mater. 2017;33(12):1429–40.
9. Hierro-Oliva M, Gallardo-Moreno AM, González-Martín ML. ToF-SIMS, contact angle and zeta potential analysis of HSA adsorption on UV-C activated Ti–6Al–4V. Mater (Basel). 2021;14(23):7416–30.
10. Barberi J, Spriano S. Titanium and protein adsorption: an overview (with ToF-SIMS insights). Front Bioeng Biotechnol. 2021;9:774125–38.
11. Barberi J, et al. Albumin and fibronectin adsorption on treated titanium and Ti–6Al–4V. Appl Surf Sci. 2022;605:154758–70.
12. Li S, Ni J, Liu X, et al. UV-modified sandblasted/acid-etched titanium: surface characteristics and biocompatibility. J Biomed Mater Res B Appl Biomater. 2012;100(6):1587–98.
13. Henningsen A, Smeets R, Heuberger R, et al. Changes in titanium and zirconia surfaces after UV or non-thermal plasma treatment. Eur J Oral Sci. 2018;126(2):126–34.
14. Huang Y, Zhang H, Chen Z, Wang Y, Yang X, Yu H. Improvement in osseointegration of titanium dental implants after exposure to ultraviolet-C light for varied durations: An experimental study in beagle dogs. J Oral Maxillofac Surg. 2022;80(8):1389–97.
15. Yin C, Zhang T, Wei Q, Cai H, Cheng Y, Tian Y, Leng H, Wang C, Feng S, Liu Z. Surface treatment of 3D printed porous Ti6Al4V implants by ultraviolet photofunctionalization for improved osseointegration. Bioactive Mater. 2022;7:26–38.
16. Villapun-Puzas VM, McCulloch E, et al. Surface free energy dominates biological interactions of selective laser-melted Ti–6Al–4V. ACS Biomater Sci Eng. 2022;8(9):3811–24.
17. Aita H, Hori N, Takeuchi M, et al. Effect of UV functionalization of titanium on osteoblast behavior and integration. Biomaterials. 2009;30(6):1015–25.
18. Att W, Ogawa T. Biological aging of implant surfaces and restoration by UV treatment. Int J Oral Maxillofac Implants. 2012;27(4):753–61.
19. Rupp F, Liang L, Geis-Gerstorfer J, Scheideler L, Hüttig F. Surface characteristics of dental implants: a review (wettability/aging). Dent Mater. 2018;34(1):40–57.
20. Aita H, Hori N, Takeuchi M, et al. The effect of ultraviolet functionalization of titanium on integration with bone. Biomaterials. 2009;30(6):1015–25.
21. Komatsu K, Kido D, Ogawa T. Reimagining bonding interfaces: UV photofunctionalization paradigm. J Dent Res. 2025;104:125–38.
22. Suzumura T, Matsuura T, Komatsu K, Ogawa T. Vacuum ultraviolet light photofunctionalization to overcome biological aging of titanium. Int J Mol Sci. 2023;24(3):1978.
23. Tominaga H, Hirata H, Koyama H, et al. UV photofunctionalization of titanium instrumentation in lumbar fusion: non-randomized controlled trial. BMC Musculoskelet Disord. 2019;20:211–22.
24. Tominaga H, Hirata H, Koyama H, et al. The effect of ultraviolet photofunctionalization of titanium instrumentation in lumbar fusion: a non-randomized controlled trial. BMC Musculoskelet Disord. 2019;20:211.
25. Choi SH, Jeong WS, Cha JY, et al. Time-dependent effects of ultraviolet and nonthermal atmospheric pressure plasma on the biological activity of titanium. Sci Rep. 2016;6:33421.
26. Gregorčič P. Comment on Bioinspired reversible switch between underwater superoleophobicity/superaerophobicity and oleophilicity/aerophilicity and improved antireflective property on the nanosecond laser-ablated superhydrophobic titanium surfaces. ACS Appl Mater Interfaces. 2020;13(2):2117–27.
27. Despotović I, Petrović Ž, Katić J, Mikić D. Alendronate as bioactive coating on titanium surfaces: an investigation of CaP–alendronate interactions. Materials. 2024;17(11):2703.
28. Kamo M, Kyomoto M, Miyaji F, et al. Time course of surface characteristics of alkali-/heat-treated titanium during vacuum storage (carbon re-accumulation). J Biomed Mater Res B Appl Biomater. 2017;105(6):1453–60.

29. de Avila ED, de Molon RS, Vergani CE, et al. Effect of UV-photofunctionalization on oral bacterial attachment and biofilm formation to titanium implant material. PLoS ONE. 2015;10(11):e0143132.
30. Mehl C, Kern M, Neumann F, et al. Effect of ultraviolet photofunctionalization of dental titanium implants on osseointegration. J Zhejiang Univ Sci B. 2018;19(7):525–34.
31. Chang LC, Wang W, Hsu M-L. Clinical applications of photofunctionalization on dental implants. J Clin Med. 2022;11(20):6047.
32. Suzumura T, Matsuura T, Komatsu K, Ogawa T. Decomposing organic molecules on titanium with vacuum ultraviolet light for rapid photofunctionalization. J Funct Biomater. 2022;14(1):11–21.
33. Cardarelli A. Reducing osseointegration time using UV machine implants treatment: clinical report. J Oral Med Dent Res. 2023;4(2):1–10.
34. Mosmann T. Rapid colorimetric assay for cellular growth and survival. J Immunol Methods. 1983;65(1–2):55–63.
35. Dominici M, Le Blanc K, Mueller I, et al. Minimal criteria for defining multipotent mesenchymal stromal cells. Cytotherapy. 2006;8(4):315–7.
36. Livak KJ, Schmittgen TD. Analysis of relative gene expression data using real-time quantitative PCR and the 2^−ΔΔCt method. Methods. 2001;25(4):402–8.
37. Schindelin J, Arganda-Carreras I, Frise E, et al. Fiji: an open-source platform for biological-image analysis. Nat Methods. 2012;9(7):676–82.
38. Simonsen JL, Rosada C, Serakinci N, et al. Telomerase expression extends proliferative life-span and maintains osteogenic potential of human BM stromal cells. Nat Biotechnol. 2002;20(6):592–6.
39. Elseberg C, Leber J, Weidner T, Czermak P. The challenge of human mesenchymal stromal cell expansion: current and prospective answers. New Insights into cell culture technology. InTech; 2017. https://doi.org/10.5772/66901.
40. International Organization for Standardization. ISO 10993–5: 2009 Biological evaluation of mdeical devices, Part 5: Tests for in vitro cytotoxicity.
41. Skårn M, Noordhuis P, Wang MY, Veuger M, Kresse SH, Egeland EV, Micci F, Namløs HM, Håkelien AM, Olafsrud SM, Lorenz S. Generation and characterization of an immortalized human mesenchymal stromal cell line. Stem Cells Dev. 2014;23(19):2377–89.
42. Kido D, Komatsu K, Suzumura T, et al. Influence of surface contaminants and hydrocarbon pellicle on wettability of titanium. Int J Mol Sci. 2023;24(19):14688–99.

Publisher's note

Springer Nature remains neutral with regard to jurisdictional claims in published maps and institutional affiliations.

Prof. Dr. Mohamed Alkhodary Mohamed Ahmed Abd ALLAH Alkhodary is currently a Professor in the Prosthetic Dental Sciences Department at the College of Dentistry, Qassim University, Saudi Arabia, and the Faculty of Dentistry, Alexandria University, Egypt. He was graduated with honor in 1999 from Alexandria University, Egypt and went on to obtain his master's degree in 2006 from the same university. In 2010, he has obtained his PhD in Prosthodontics from Alexandria University in joint supervision with Princeton University in USA where He was appointed as a visiting research collaborator at the mechanical and aerospace engineering department in 2008. He is an ex-head of the Department of Prosthetic Dental Sciences, Qassim University from 2016 to 2019, the head of Research Laboratories Management Unit, and the head of the students' research and presentation skills supervision committee at the same college. His research expertise encompasses removable prosthodontics, dental implantology, and tissue engineering scaffolds fabrication and characterization, bone bioengineering, experimental animal surgery, and laser micro-grooving of dental implants. Additionally, he is a member of the Tissue Engineering and Regenerative Medicine International Society (TERMIS), Egyptian dental association, and the Saudi Commission for Health Specialties (SCHS). He was a member in 9 finished international research projects, and a principal investigator in 2 more.